*Article*

# Variable Stiffness Design and Multiobjective Crashworthiness Optimization for Collision Post of Subway Cab Cars

**Wei Guo** [1,2,3], **Ping Xu** [1,2,3], **Zhaofeng Yi** [4], **Jie Xing** [1,2,3], **Hui Zhao** [1,2,3] and **Chengxing Yang** [1,2,3,*]

1   Key Laboratory of Traffic Safety on Track, Ministry of Education,
    School of Traffic & Transportation Engineering, Central South University, Changsha 410075, China;
    194212077@csu.edu.cn (W.G.); xuping@csu.edu.cn (P.X.); xingjie@csu.edu.cn (J.X.);
    164211033@csu.edu.cn (H.Z.)
2   Joint International Research Laboratory of Key Technology for Rail Traffic Safety,
    Central South University, Changsha 410075, China
3   National & Local Joint Engineering Research Center of Safety Technology for Rail Vehicle,
    Central South University, Changsha 410075, China
4   Technology Research Center, CRRC Tangshan Co., Ltd., Tangshan 064000, China; yizhaofeng@tangche.com
*   Correspondence: Chengxing_Yang_Hn@csu.edu.cn

**Abstract:** This paper proposes a variable stiffness collision post (VSCP) structure based on a uniform stiffness collision post (USCP) structure and performs stiffness matching optimization for VSCPs. A collision post structure assembled in a subway front-end frame can maintain the living space and absorb a certain amount of the kinetic energy of an impact. The experiment was applied on USCP, and the finite element model was verified experimentally. To investigate the effects of the stiffness parameters of VSCP on the specific energy absorption response (SEA_VSCP) and the area of intrusion response (S_In), response surface models fitted from design of experiment were adopted with the finite element model. In addition, a multiobjective optimization design was realized by using the global response search method and a Pareto frontier sequence was generated, which was based on the developed response surface model. It was found that the optimal value of SEA_VSCP and S_In responses cannot be achieved at the same time. Finally, a grey relational analysis is propounded to attain a desirable balance between SEA_VSCP and S_In from the Pareto frontier sequence under constraints of the peak crash force of VSCP and energy absorption of the front-end of cab car. The optimization result shows that the crashworthiness of VSCP is better than that of USCP.

## 1. Introduction

The rapid development of subway traffic has led to an increase in subway vehicle collision accidents, which will inevitably cause serious casualties and property losses [1,2]. The study of railway vehicle passive safety technologies has become a new hot topic [3,4]. Recently, thin-walled structures have been widely used as energy absorption devices due to their low masses and high energy absorption efficiencies. There are many research results demonstrating the excellent crashworthiness performance of thin-walled structures [5–9]. Collision post structures as thin-walled structures also have all the merits mentioned above. Subway cab cars are located at the very end of railway passenger-carrying vehicles. If a collision accident occurred, the subway operator working in cab car would face a great risk of injury and even death. Passengers in this subway would also be severely hurt. On the afternoon of 22 June 2009, a subway train-on-train collision occurred in Northeast Washington, D.C., United States. A stopping train was crashed into by a moving train behind of it, resulting the death of the train operator and eight passengers and the injuries of 80 people, and making it the most serious crash in the history of the Washington Metro [10].

In this accident, the living space of cab cars was severely damaged, leading to the death of Metro operators.

At present, after many studies on the crashworthiness of subway underframe structures, subway underframes have a great amount of energy absorption capacity [11–19]. However, if the train climbs onto the other train, leading to partial or no contact between the two trains' underframes in a collision, the energy absorption structure of the underframe cannot effectively function to dissipate the collision kinetic energy, and then the superstructure will bear a full and huge impact load. In the Washington Metro crash accident, the subway underframe provided very limited protection in this scenario. Therefore, further research on the superstructure above the underframe is needed. Xing [20] proposed a new collision post structure aimed at improving the crashworthiness of subway cab cars. This new structure has two innovative characteristics: (1) a simpler junction between the post and the car roof, which can reduce the stress concentration of joints by giving a more reasonable load transfer path; (2) a new stiffness design that induces an ideal deformation mode to maintain the living space of cab cars. Kang [21] performed an optimization design for an FXD-3-type passenger electric locomotive cab and studied the responses of cab cars loaded at the bottom, middle and top under compression conditions. Through numerical simulation and static strength experimental analysis, the results show that the steel structures of a cab car are in line with the requirements of standard EN12663. Based on ASME RT-2 2014, Liu [22] studied the elastic-plastic deformation law of collision posts located at the end of subway vehicles. Through finite element model analysis and test verification, it was determined that the elastic-plastic performance of the collision post could meet the requirements of ASME RT-2 2014. There are also some studies on increasing the strength of cab cars. Tyrell [23] conducted a study to evaluate the effectiveness of structural modifications for increasing crashworthiness in train collisions. The influence of the modifications on weight and manufacturing cost of vehicle was also estimated. Mayvilie [24] studied the results of an experimental study to determine the strength and energy absorption capability of cab car rail vehicle corner structures which were built to meet strength demands and for structures reformed to bear higher loads and absorb more energy. As mentioned above, much research for strengthening the crashworthiness of cab cars is currently aiming at protecting the safety of operators in cab cars. Since the Washington Metro accident, the study of the strength of superframes, especially for collision post structures, has become increasingly necessary. For collision post structures included in the superframe, the function can be illuminated as follows: (1) the collision post structure should be able to maintain the living space of cab cars; (2) the collision post structure should absorb as much energy as possible with very limited displacement. However, these are conflicting objectives; that is, the more energy absorbed, the greater the lateral displacement or the larger the buckling deformation of the collision post, and the larger the plastic deformation of the collision post, the smaller the living space in cab cars. Hence, making full use of the limited displacement of collision posts to balance these two goals has become a difficulty for crashworthiness optimization. Therefore, this article puts forward the design of a VSCP. An optimization for stiffness matching was performed to improve the crashworthiness of the collision post.

In this paper, a stiffness matching optimization strategy to improve the crashworthiness of collision posts under lateral dynamic impact is performed. This paper starts with the initial model details and experiment in Section 2 and proposes crashworthiness indices. Subsequently, the numerical simulation model, which is in parallel with the experiment, is proposed in Section 3, and the finite element model (FEM) was verified by experimental data. Then, in Section 4, a full second-order response surface (RS) surrogate model is established with an experimental design, and parameterized research and analysis are carried out. The prediction expressions for SEA_VSCP and S_In are analytically constructed. In Section 5, the global response search method (GRSM) as the optimization algorithm was employed for VSCP to generate Pareto frontier for conflicting objectives. Grey relational analysis is implemented to hit the trade-off from the Pareto frontier. Balance is found

among living space, energy absorption, and light weight. The optimum matching strategy for stiffness distribution for collision post structure is obtained so that crashworthiness of a subway cab car is improved. Conclusions are drawn in Section 6.

## 2. Model Details and Experiment

### 2.1. Specimen and Material Properties

The energy absorption collision post for the bilevel subway cab car displayed in Figure 1b is composed of four parts with thin-wall rectangular tubes, as follows: Part I at the top, Parts II and III at the middle, and Part IV at the bottom. There are four stiffening diaphragms in Part IV of each collision post to reinforce the strength. In this paper, the effects of diaphragms are not studied. The thickness of each part is 9.5 mm, so the initial structure is USCP. The information for USCP can be seen in Figure 1c.
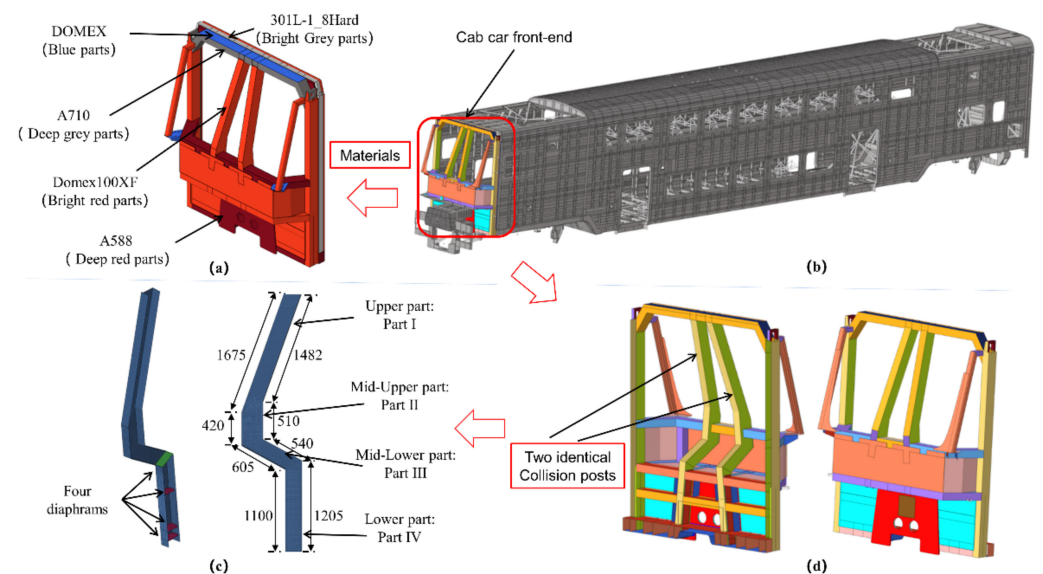


**Figure 1.** Details for cab car front-end and USCP: (**a**) materials of the cab car front-end; (**b**) bilevel subway car; (**c**) details of USCP; (**d**) cab car front-end of a bilevel subway car.

Several different materials are used in the cab car front-end. As shown in Figure 1a, the bright grey and deep grey parts are 301 L-1_8Hard and A710, respectively. The material of the blue parts is DOMEX, and the materials of the deep red and bright red parts are A588 and cra-Domex100XF.

The collision posts are made of car-Domex100XF. For exploring the material properties, quasi-static tensile tests were carried out. Three specimens with standard dimensions were stretched using an MTS 647 hydraulic tensile test machine, which is shown in Figure 2. The stress–plastic strain curve shown in Figure 3 was obtained from the record of MTS 647. The material properties of USCP are listed in Table 1.

**Table 1.** Material property parameters.

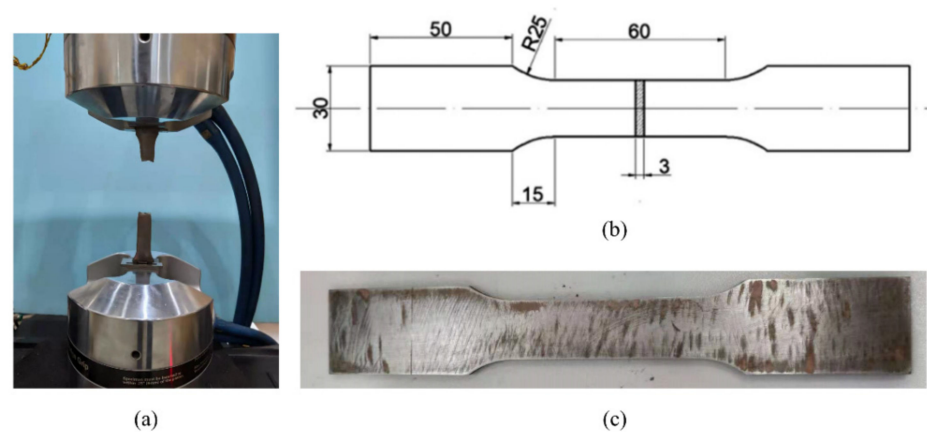| Mechanical Parameters | Units | Values |
|:---:|:---:|:---:|
| Density | kg/m$^3$ | 7800 |
| Young's modulus | GPa | 207 |
| Poisson's ratio | / | 0.3 |
| Yield stress | GPa | 690 |

**Figure 2.** Tensile test machine and the specimen: (**a**) MTS 647 hydraulic tensile test machine; (**b**) dimensions of specimen; (**c**) physical specimen.
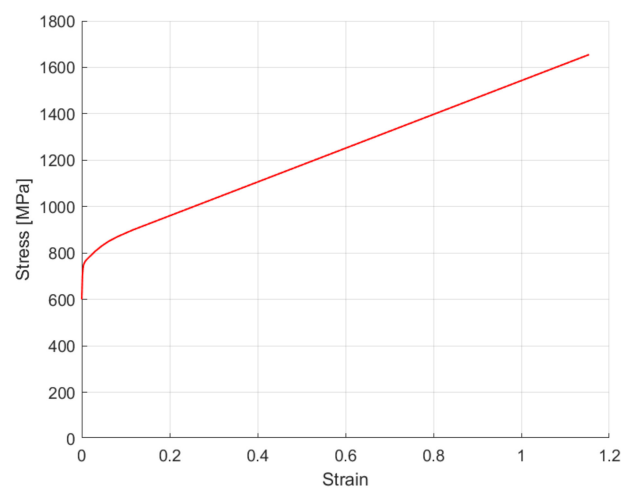


**Figure 3.** Stress–plastic strain curve.

### 2.2. Experimental Setup Details

In this experiment, the test article is comprised of the front-end structure of the cab car, a sidewall post and a mounting structure for attachment to the rigid wall. As shown in Figure 4b, the test article was fixed on a rigid wall, and a dynamic crash was loaded by a test trolley with an impact ram. The crash location is shown in Figure 4d, and the lateral offset is 364 mm between the center of the test article and the center of the rigid wall, which is aimed to impact one of USCPs. A velocity of 4.69 m/s was applied for the test trolley, and the total impact mass was 24,662 kg, including the test trolley and impact ram.

### 2.3. Crashworthiness Indicators

The energy absorption capacity is a basic requirement for the design of collision posts. The peak collision force is also a main indicator for bursting great deceleration injury on passenger in accident. Living space is a key indicator for operators' survival. Therefore, considering the lightweight design, we selected indices such as specific energy absorption (SEA), area of intrusion (S_In), energy absorption (EA) and peak crushing force (PCF), which are specified as follows:

**Figure 4.** Experimental setup: (**a**) test trolley; (**b**) measurement devices; (**c**) crash location; (**d**) test article location.

(1) EA as the first index can be calculated as follows [25]:

$$\text{EA} = \int_0^S F(s)ds \tag{1}$$

where *F*(*s*) is the continuous crashing force and *S* is crashing displacement.

(2) The second index is SEA, indicating the EA per unit mass [26], and SEA can be calculated as follows:

$$\text{SEA} = \frac{\text{EA}}{\text{M}} \tag{2}$$

where M is the total mass of collision posts.

(3) PCF is the maximum value of *F*(*s*) during the collision process [12], which is vital to determine the occupant's survival rate.

S_In is the intrusion area during crash and can be calculated with the area enclosed by the markers. Ten markers are defined in Figure 5a, and the heights of the markers from bottom to top are 0, 400, 800, 1000, 1200, 1600, 2000, 2400, 2800 and 3100 mm. Marker 1 is on the underframe of cab car front-end. From Figure 5b, we can see that in the horizontal direction, each marker has two positions that denote the positions before and after crash. The distance between two positions of a marker is the deformation of the collision post at this marker. Thus, the S_In response can be calculated with the functions in Equation (3):

$$\text{S\_In} = \sum_{i=1}^{9} S_i = \sum_{i=1}^{9} \frac{(a_i + b_i)h_i}{2} \tag{3}$$

where $a_i$, $b_i$ and $h_i$ are the length of the upper base and lower base and the height of each trapezoid, respectively.
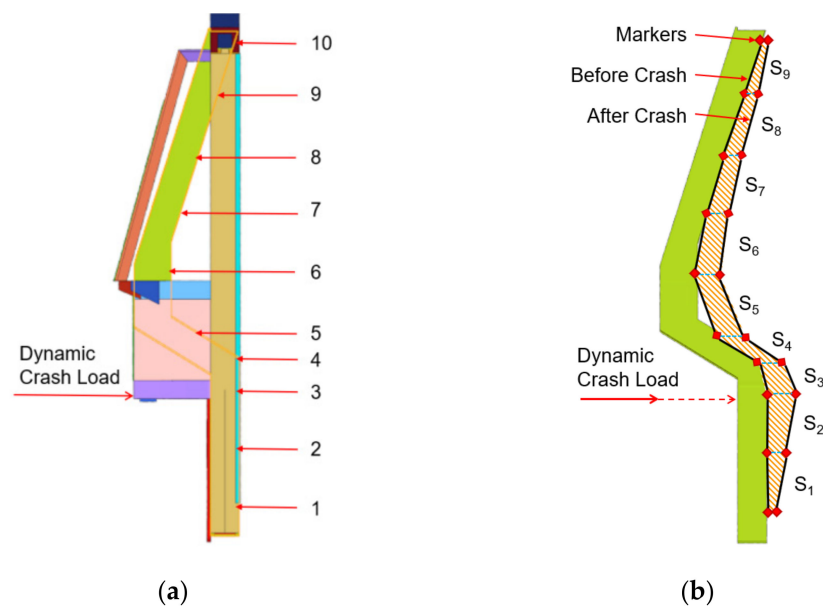
(**a**)　　　　　　　　　　(**b**)

**Figure 5.** Longitudinal deformation details: (**a**) location of markers; (**b**) S_In sketch.

## 3. Numerical Simulations

### 3.1. Finite Element Model

In this study, a numerical simulation was conducted using the explicit nonlinear finite element package LS-DYNA. The FEM was established using the following parts: test trolley and rail [27], impact ram, and cab car front-end frame with two USCPs, which is shown in Figure 6. A Belytschko-Tsay shell element with five-point integration is adopted to accelerate the numerical calculation. The mesh size of all the structures of the cab car front-end is 10 mm. For the test trolley, which is set up as a rigid body, the mesh size was 50 mm, as were rails. The mesh size of 20 mm was adopted on impact ram. For the FEM, three types of contact algorithms were employed in the calculation. As shown in Figure 7, the automatic_surface-to-surface contact algorithm was employed to the impact ram and the underframe of cab car front-end, the tied_surface-to-surface_offset was employed to wheel and test trolley, and the automatic_single_surface was applied on the excluded parts of the FEM. The test article was installed on a rigid wall, and the friction factor between them was 0.3. "*MAT_PIECEWISE_LINEAR_PLASTICITY" is applied from LS-DYNA material library, and the material is defined by the data from tensile tests. Moreover, initial penetration must be avoided to maintain energy conservation during modeling.
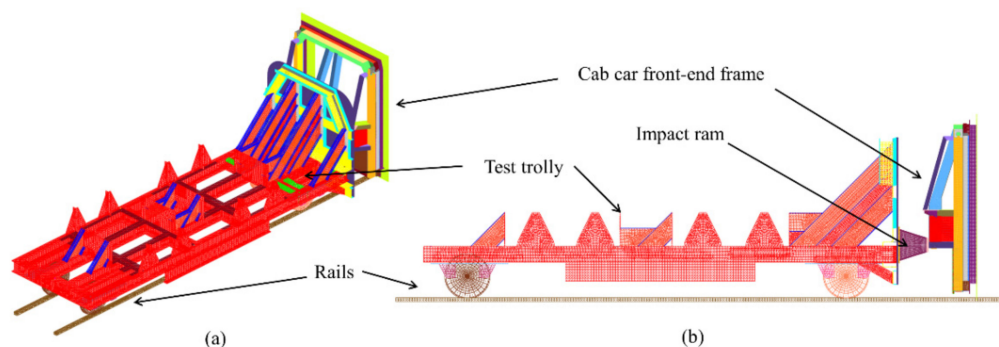


(a)　　　　　　　　　　(b)

**Figure 6.** Finite element model: (**a**) isometric view; (**b**) Left view.
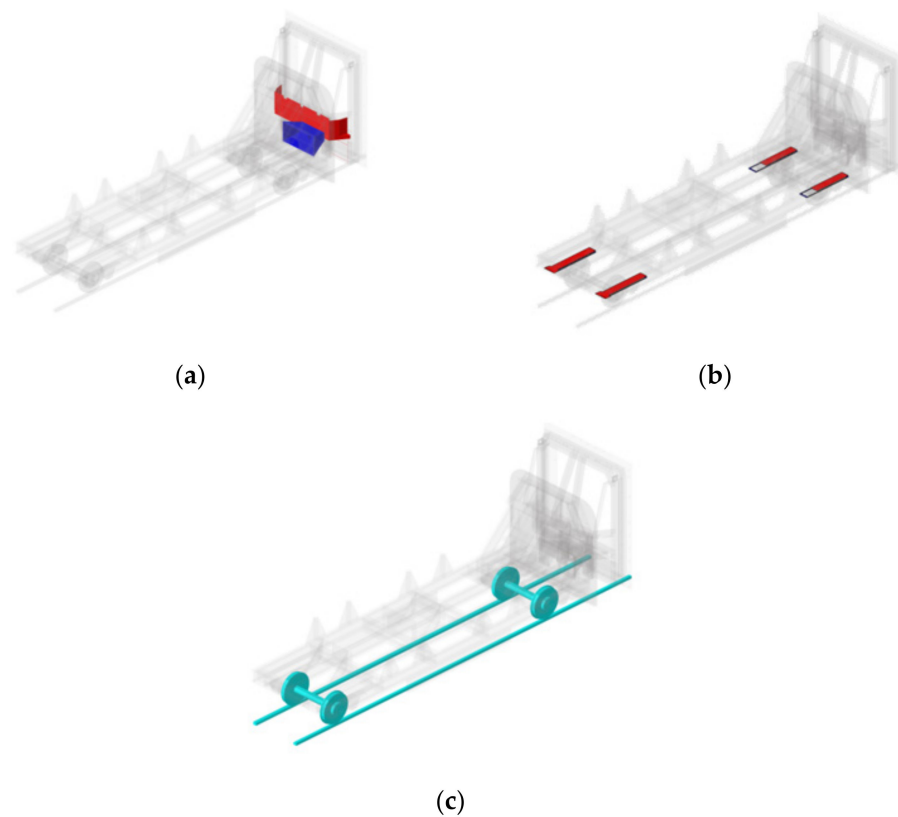
(a)　　　　　　　　　　　　　　　　　　　　　(b)



(c)

**Figure 7.** Surface-to-surface contact algorithm: (**a**) impact ram and cab car front-end; (**b**) wheel and test trolley; (**c**) wheel and rail.

### 3.2. Validation of FEM

To analyze the FEM validation of the USCP, the discussion between the simulation and experiment in deformation mode, permanent longitudinal displacement of 10 markers, and energy absorption and the analysis of energy curves are described as follows.

Figure 8 shows the deformation comparison between the experiment and simulation. The finite element simulation results well restored the deformation captured in the experiment. The permanent longitudinal displacement for 10 marks between the experiment and simulation are plotted in Figure 9. The positions of the 10 markers along the collision post almost coincide in Figure 9b, and a detailed value comparison between them is shown in Figure 9c with a bar chart.

The energy is calculated by the kinetic energy theorem in Table 2. The error of the rebound velocity between the experiment and simulation is 2.979%, and the error of the final energy absorption is 2.347%, which is in a reasonable range.

**Table 2.** Velocity and Energy.

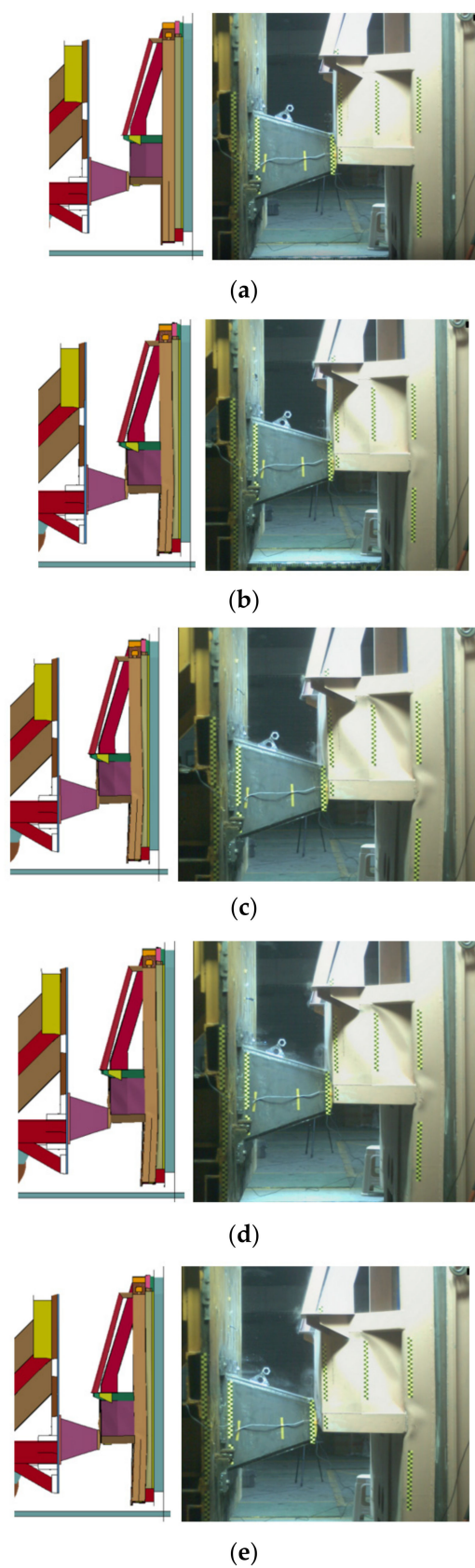|  | Test | Simulation | Error |
|---|---|---|---|
| Crash velocity (m/s) | 4.69 | 4.69 | / |
| Rebound velocity (m/s) | 2.182 | 2.117 | 2.979% |
| Total mass (kg) | 24,662 | 24,662 | / |
| Energy (MJ) | 0.213 | 0.208 | 2.347% |

**Figure 8.** Deformation comparison between the simulation and experiment: (**a**) t = 0, simulation: 0, experiment: 0; (**b**) t = 16 ms, simulation: 47.8 mm, experiment: 49.142 mm; (**c**) t = 25 ms, simulation: 55.1 mm, experiment: 59.317 mm; (**d**) t = 33 ms, simulation: 48 mm, experiment: 50.488 mm; (**e**) t = 49 ms, simulation: 33.6 mm, experiment: 31.577 mm.
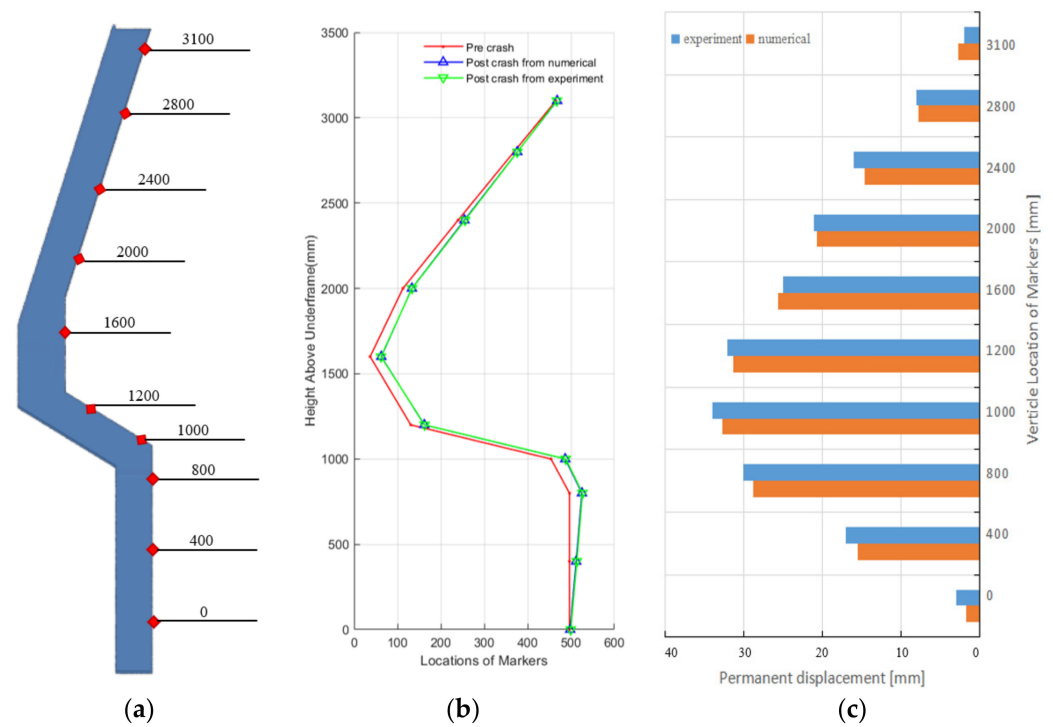
**Figure 9.** Longitudinal displacement comparison between the experiment and simulation: (**a**) permanent displacement along the collision post vertically; (**b**) permanent longitudinal displacement at the location of 10 markers. (**c**) detailed displacement comparison for every marker before and after crash.

Figure 10 presents the energy curves, including kinetic energy, internal energy, total energy and hourglass energy. The energy absorbed by cab car front-end is 0.208 MJ in numerical simulation and 0.213 MJ in the experiment, so the error between them is 2.347%, which is acceptable. The residual kinetic energy of the test trolley with ram is 55.264 kJ in the numerical simulation and 58.709 kJ in the experiment, and the error is 5.868%. It is also observed that the hourglass energy is 1.01% of the total energy, which is less than 5% of the total energy [28]. Therefore, reasonable agreement in four aspects indicated that the finite element model has a good consensus with experiment and that FEM could be used in further studies.
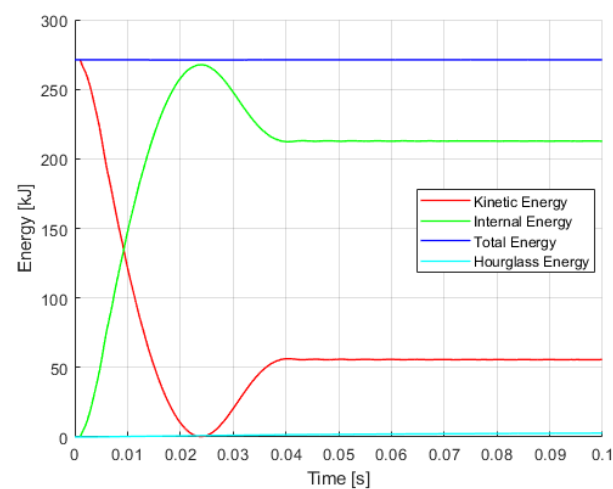


**Figure 10.** Energy curves.

## 4. Surrogate Models and Parametric Analysis

### 4.1. Design of Experiment (DOE)

Variable stiffness design is realized by varying the thickness of each part of the collision post. To investigate the influence of the stiffness of every part on crashworthiness, the FEM of the USCP post was divided into four parts, which are expressed clearly in Figure 11. It is worth noting that the process of dividing USCP does not include a remesh process. As shown in Figure 12, the green, blue, yellow and pink parts correspond to Parts I to IV, respectively, thereby VSCP structure is obtained. The thicknesses of the upper part (Part I), mid-upper part (Part II), mid-lower part (Part III) and lower part (Part IV) of the collision post were set as design variables A, B, C and D, respectively. The DOEs were created based on a three-level Box-Behnken design [29]. The efficiency of the Box-Behnken design is slightly higher than the central composite design, but much higher than the three-level full factorial design [30]. Table 3 shows the specific values used in the experiments. SEA_VSCP, S_In, energy absorption of the front-end of cab car (EA_FE) and the peak crash force of VSCP (PCF_VSCP) are selected as design responses. The design variables and corresponding calculated responses are listed in Table 4.

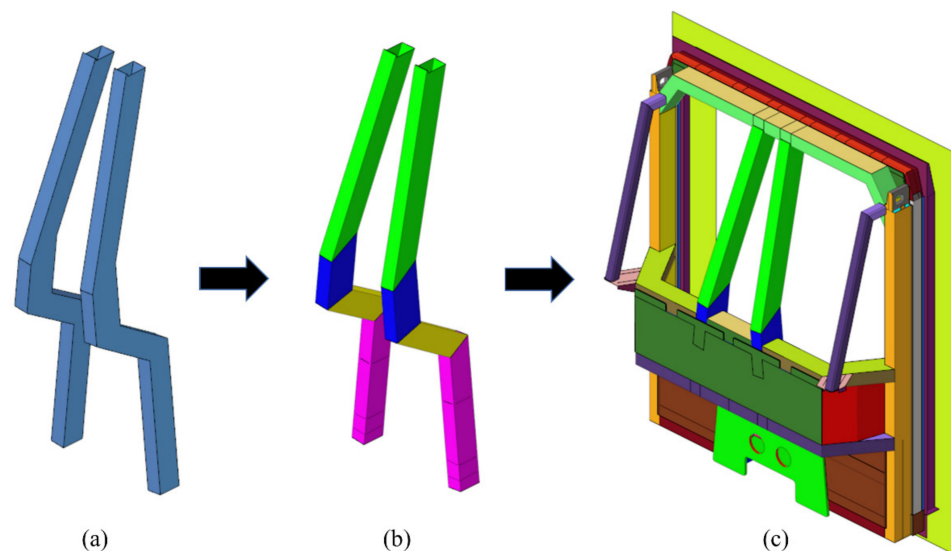

(a)　　　　　　　　　(b)　　　　　　　　　(c)

**Figure 11.** Finite element model for VSCP: (**a**) USCP; (**b**) VSCP; (**c**) cab car front-end with VSCP.
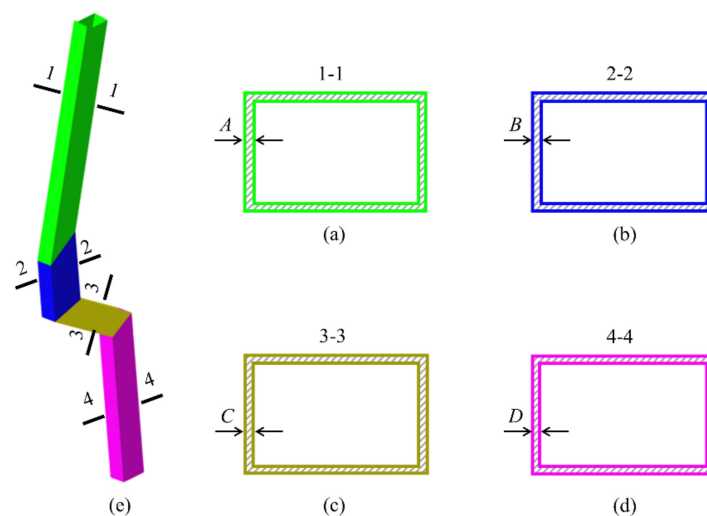


**Figure 12.** Parameters of thickness for VSCP: (**a**) thickness of Part I and parameter A; (**b**) thickness of Part II and parameter B; (**c**) thickness of Part III and parameter C; (**d**) thickness of Part IV and parameter D; (**e**) VSCP model.

**Table 3.** Thickness parameters and experimental design levels.

| Thickness Parameters | Code | −1 | 0 | 1 |
|---|---|---|---|---|
| Thickness of Part I | A | 5.0 | 9.5 | 14.0 |
| Thickness of Part II | B | 5.0 | 9.5 | 14.0 |
| Thickness of Part III | C | 5.0 | 9.5 | 14.0 |
| Thickness of Part IV | D | 5.0 | 9.5 | 14.0 |

**Table 4.** Design of experiment and simulation results of VSCP.

| Std. | Thickness Parameters | | | | Responses | | | |
|---|---|---|---|---|---|---|---|---|
| | A (mm) | B (mm) | C (mm) | D (mm) | SEA_VSCP (kJ) | S_In (mm$^2$) | EA_FE (kJ) | PCF_VSCP (kN) |
| 1 | 5 | 5 | 9.5 | 9.5 | 20.4927 | 62,589.432 | 213.12 | 5446.6989 |
| 2 | 5 | 14 | 9.5 | 9.5 | 23.0703 | 57,814.749 | 212.197 | 5517.7271 |
| 3 | 14 | 5 | 9.5 | 9.5 | 21.3100 | 63,570.481 | 213.131 | 5482.8599 |
| 4 | 14 | 14 | 9.5 | 9.5 | 24.1989 | 59,263.441 | 213.196 | 5544.4636 |
| 5 | 5 | 9.5 | 5 | 9.5 | 22.1219 | 63,277.74 | 217.861 | 5171.6082 |
| 6 | 5 | 9.5 | 14 | 9.5 | 23.7490 | 59,637.754 | 212.906 | 5531.1088 |
| 7 | 14 | 9.5 | 5 | 9.5 | 22.3060 | 66,576.92 | 217.691 | 5204.1427 |
| 8 | 14 | 9.5 | 14 | 9.5 | 25.349 | 59,480.653 | 213.245 | 5573.385 |
| 9 | 5 | 9.5 | 9.5 | 5 | 31.6865 | 61,808.56 | 220.188 | 5039.2488 |
| 10 | 5 | 9.5 | 9.5 | 14 | 19.5427 | 60,593.651 | 212.091 | 5602.5853 |
| 11 | 14 | 9.5 | 9.5 | 5 | 31.8235 | 63,315.237 | 220.026 | 5043.4856 |
| 12 | 14 | 9.5 | 9.5 | 14 | 21.0165 | 61,016.728 | 212.63 | 5630.2207 |
| 13 | 9.5 | 5 | 5 | 9.5 | 21.2040 | 65,329.503 | 217.663 | 5168.0469 |
| 14 | 9.5 | 5 | 14 | 9.5 | 22.7954 | 61,696.916 | 213.111 | 5516.544 |
| 15 | 9.5 | 14 | 5 | 9.5 | 22.6148 | 63,286.588 | 217.191 | 5217.6989 |
| 16 | 9.5 | 14 | 14 | 9.5 | 25.8719 | 56,924.963 | 213.075 | 5584.1214 |
| 17 | 9.5 | 5 | 9.5 | 5 | 30.7063 | 65,535.246 | 220.268 | 5015.0507 |
| 18 | 9.5 | 5 | 9.5 | 14 | 18.4966 | 61,664.09 | 212.689 | 5579.529 |
| 19 | 9.5 | 14 | 9.5 | 5 | 32.0334 | 63,002.815 | 219.962 | 5052.5604 |
| 20 | 9.5 | 14 | 9.5 | 14 | 21.7133 | 57,000.466 | 212.362 | 5651.6439 |
| 21 | 9.5 | 9.5 | 5 | 5 | 29.1332 | 67,094.875 | 219.539 | 5002.3575 |
| 22 | 9.5 | 9.5 | 5 | 14 | 18.9549 | 62,508.464 | 216.981 | 5272.4815 |
| 23 | 9.5 | 9.5 | 14 | 5 | 32.8472 | 64,518.289 | 220.661 | 5040.4061 |
| 24 | 9.5 | 9.5 | 14 | 14 | 19.36247 | 58,380.467 | 210.191 | 5777.7708 |
| 25 | 9.5 | 9.5 | 9.5 | 9.5 | 22.95254 | 58,726.779 | 212.732 | 5510.8116 |

*4.2. Establishment and Accurate Evaluation of Surrogate Models*

Based on the DOE results, full quadratic RS models were established. Three common numerical indices, the average relative error (ARE), maximum relative error (MRE), and coefficient of determination ($R^2$), were employed to verify the accuracy of RS models. ARE, MRE, and $R^2$ can be calculated with Equations (5)–(7), respectively:

$$\mathrm{ARE} = \frac{\sum \frac{|\hat{y}_i - y_i|}{y_i}}{n} \times 100\% \tag{4}$$

$$\mathrm{MRE} = Max\left(\frac{|\hat{y}_i - y_i|}{y_i}\right) \times 100\% \tag{5}$$

$$\mathrm{R}^2 = 1 - \frac{\sum(\hat{y}_i - y_i)^2}{\sum(\hat{y}_i - \overline{y}_i)^2} \tag{6}$$

where $\hat{y}_i$ and $\overline{y}_i$ are the corresponding predicted by RS models and mean values for the finite element analysis values $y_j$ at each checking point $j$, respectively; and n is the sum of checking points. Generally, the RS model is more accurate with a smaller ARE and MRE as well as a larger $R^2$ value.

Table 5 displays the details of five randomly selected points, and the errors among three fit specifics are summarized in Table 6. The results reveal that full quadratic models are proposed and the corresponding polynomial functions for SEA_VSCP and S_In are attached in Appendix A: Polynomial functions of SEA_VSCP and S_In.

**Table 5.** Details of five arbitrarily selected test points.

| Std. | Thickness Parameters | | | |
|:---:|:---:|:---:|:---:|:---:|
| | A (mm) | B (mm) | C (mm) | D (mm) |
| 1 | 12.763892 | 5.0492977 | 10.245132 | 8.9565827 |
| 2 | 8.9680140 | 9.5619450 | 11.151149 | 6.4011006 |
| 3 | 5.9441867 | 13.780611 | 13.022969 | 12.452696 |
| 4 | 7.5545501 | 11.198215 | 6.0056417 | 8.4904300 |
| 5 | 11.633395 | 7.2132390 | 8.0068415 | 11.175257 |

**Table 6.** Error analysis of the RS models.

| Objective | Fit Specifics | ARE (%) | MRE (%) | $R^2$ |
|:---:|:---:|:---:|:---:|:---:|
| | Squared | 5.7627 | 11.2748 | 0.9403262 |
| SEA_VSCP (kJ/kg) | Cubic | 5.3546 | 9.7011 | 0.9477829 |
| | Full Quadratic | 3.5395 | 6.6024 | 0.9744627 |
| | Squared | 0.7332 | 2.1796 | 0.9067982 |
| S_In ($mm^2$) | Cubic | 0.6954 | 2.1249 | 0.9205400 |
| | Full Quadratic | 0.6519 | 1.9937 | 0.9312412 |

*4.3. Parametric Study*

4.3.1. Effect of Thickness on S_In Response

The curves in Figure 13 show the effect of parameters on the S_In response. The slope of curve represents the influence of parameters on responses; the greater the slope, the greater the influence. Compared with parameter A, parameters B, C and D with larger slopes have more distinct effects on S_In. This phenomenon manifests as no obvious deformation, which is mainly due to the distance between Part I and the crash location being greater than that of the other three parts. It can also be noted that all the curves undergo a process in which with increasing A, B, C and D, the value of S_In response decreases and then increases, which is more apparent for the effect of A. The stiffness of cab car front-end structures except for the VSCP (CFSV) is constant. The stiffness of VSCP improves with increasing A, B, C and D. If the stiffness of VSCP exceeds that of CFSV, deformation begins at CFSV when facing the crash process. This result is not desired because CFSVs are not energy absorbing structures, and the integrality of these structures is vital for living space. Figure 14 presents the response surfaces, which indicate the interaction effects of parameters B, C and D on the S_In response. A smaller amount of S_In can be realized if B, C and D are greater.
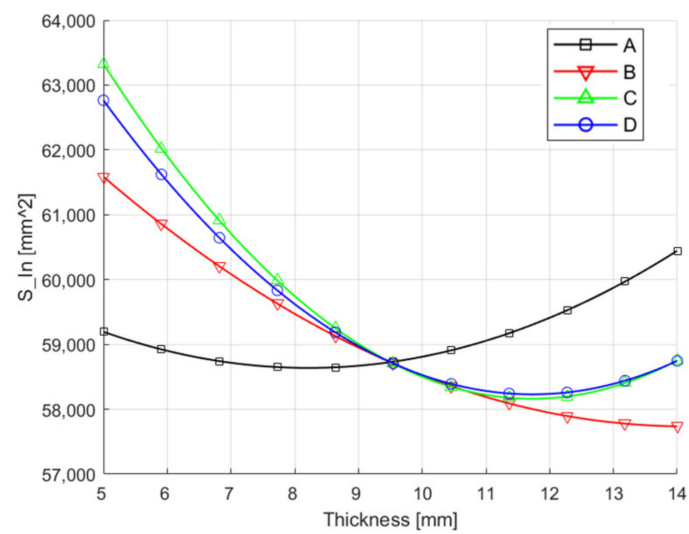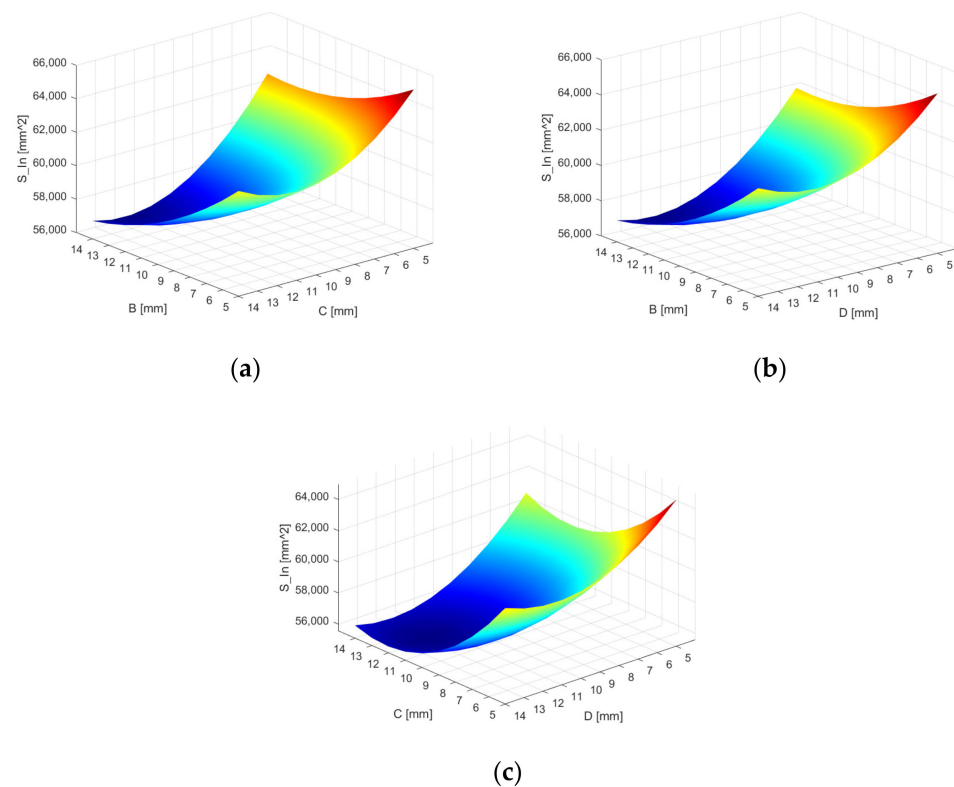
**Figure 13.** Effect of thickness on S_In response.



(**a**)

(**b**)



(**c**)

**Figure 14.** Response surfaces of S_In: (**a**) effect of thickness of parameters B and C on S_In; (**b**) effect of thickness of parameters B and D IV on S_In; (**c**) effect of thickness of parameters C and D on S_In.

### 4.3.2. Effect of Thickness on SEA_VSCP Response

To explain the influence of the design variables on SEA_VSCP more clearly, the energy absorption of the variable stiffness collision post (EA_VSCP) and the mass of the variable stiffness collision post (M_VSCP) responses were also analyzed. The effect of thickness on the energy absorption of VSCP (EA_VSCP) and the mass of VSCP (M_VSCP) responses are shown in Figure 15.
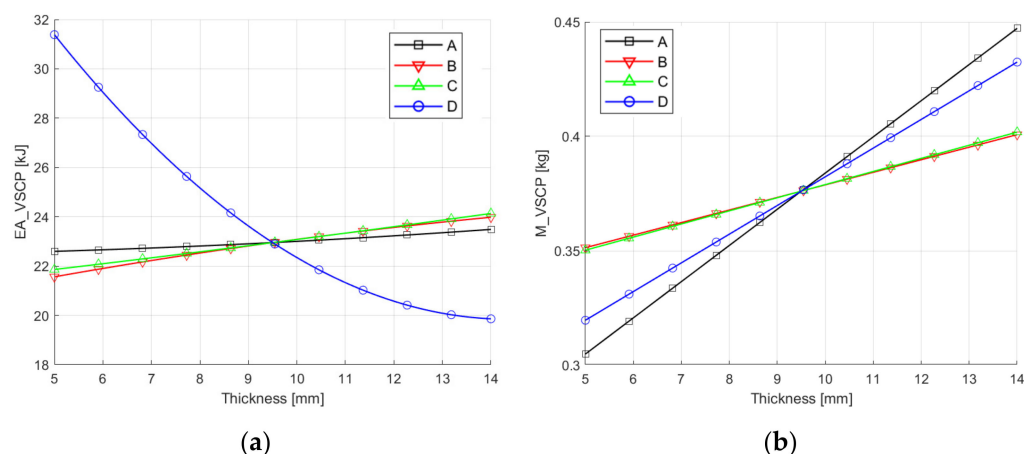
(a)          (b)

**Figure 15.** Effect curves of thickness: (**a**) Effect of parameters on EA_VSCP; (**b**) Effect of parameters on M_VSCP.

From Figure 15a, it can be seen that parameter D with the largest slope has a significant and negative effect on EA_VSCP. Parameters A, B and C with small slopes have little effect on EA_VSCP, and the curves of A, B and C are almost monotonous. It can be concluded that the energy absorbed by collision posts is mainly dissipated by the deformation of Part IV. From Figure 15b, it can be seen that parameters A and D with large slopes have obvious and positive effects on M_VSCP because Part I and Part IV are larger in size. All the linear curves indicate that parameters A, B, C and D have linear effects on M_VSCP.

The effect of parameters on SEA_VSCP is presented in Figure 16a. The slopes of the curves are D, A, C, and B in order of highest to lowest. Parameters A and D with large slopes have significant and negative effects on the SEA_VSCP response, and parameters B and C have little effect on slopes that are almost zero. This phenomenon mainly occurs because both A and D have a significant effect on M_VSCP, and A has the largest effect on EA_VSCP. Therefore, we can conclude that SEA_VSCP is less sensitive to B and C, and if Part I and Part IV became thinner, the SEA_VSCP would increase significantly, and the conclusion is presented with the response surfaces in Figure 16b.
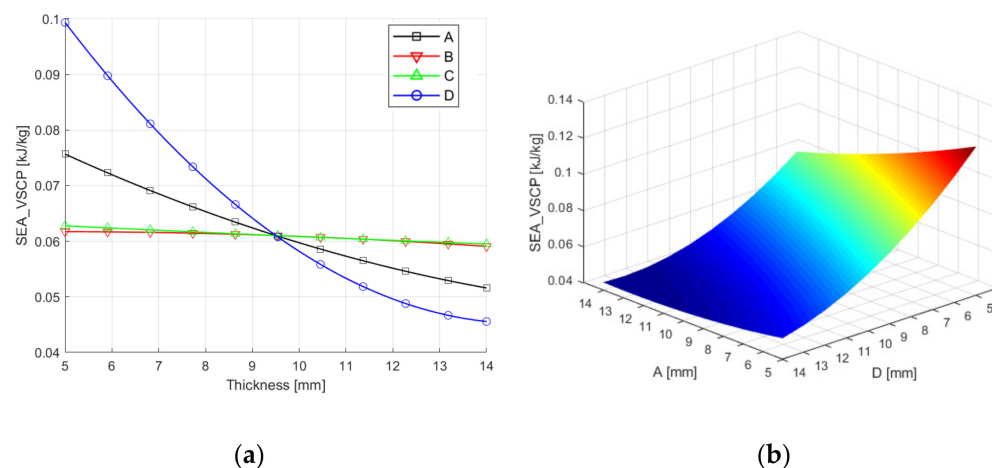


(a)          (b)

**Figure 16.** Effect of thickness on the SEA_VSCP response: (**a**) effect of single variable thickness on SEA_VSCP; (**b**) response surface of SEA_VSCP with Parameters A and D.

### 4.3.3. Effect of Thickness on PCF_VSCP and EA_FE Responses

The effect of thickness on PCF_VSCP is shown in Figure 17a. Parameters C and D with large slopes have more obvious effects on PCF_VSCP compared with parameters A and B. PCF_VSCP increases as parameters C and D increase. It is worth noting that there is a cross-point in Figure 17a with a thickness of 9.5 mm and a PCF_VSCP of 5720 kN. The effect of

thickness on EA_FE is shown in Figure 17b. By comparing Figure 17a,b, we can easily find that the trends of curves in these two figures are almost opposite, and parameters C and D with larger slopes have palpable and positive effects on EA_FE. There is also a cross-point with a thickness of 9.5 mm and an EA_FE of 213 kJ. Because the effects of parameters C and D for PCF_VSCP and EA_FE are more significant, the response surfaces affected by C and D are shown in Figure 18. In other words, it can be concluded that the relationship between the stiffness of the three parts (Part II, Part III and Part IV) and PCF_VSCP is positively correlated, and the effect of Part I is nonsignificant. The relationships between the stiffness of the two parts (Part III and Part IV) and EA_FE are negative, and the effects of Part I and Part II are nonsignificant.
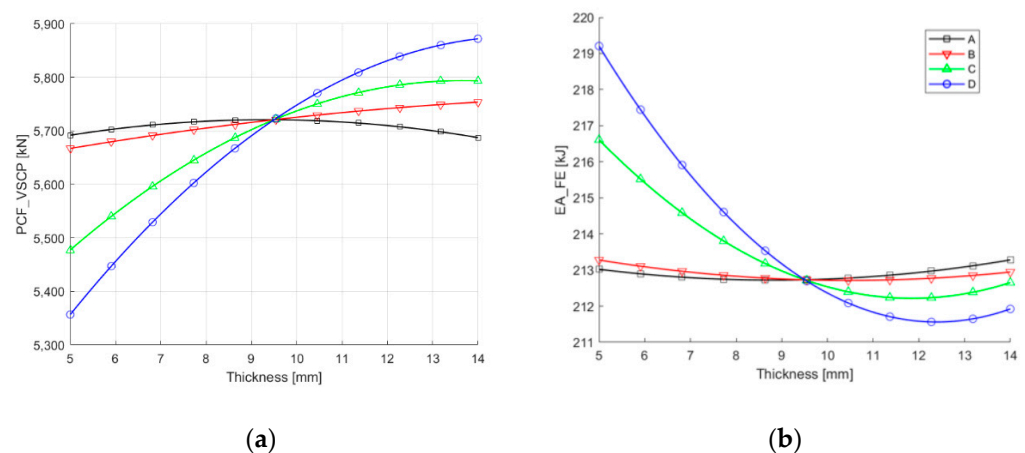


(a)　　　　　　　　　　　　　　　　　　　　　　(b)

**Figure 17.** Effect of thickness: (**a**) effect of thickness on PCF_VSCP response; (**b**) effect of thickness on EA_FE response.
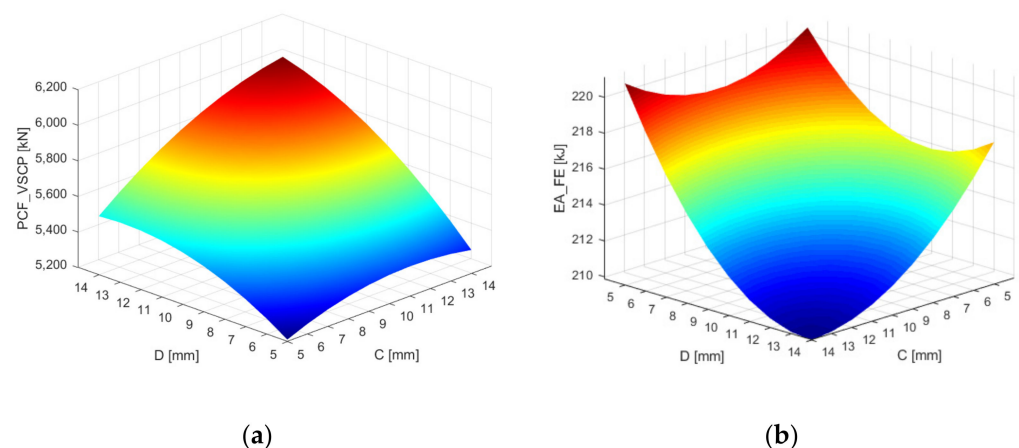


(a)　　　　　　　　　　　　　　　　　　　　　　(b)

**Figure 18.** Response surface: (**a**) response surface of PCF_VSCP with parameters C and D; (**b**) response surface of EA_FE with parameters C and D.

## 5. Multiobjective Crashworthiness Optimization Design of VSCP

*5.1. Definition of Optimization Problems*

Energy absorption structures should dissipate as much energy per unit mass; therefore, maximum SEA_VSCP was selected as the first objective function [13]. S_In was adopted as the other objective function because it denotes the destruction extent of occupants' living space. Moreover, to avoid severe injuries or deaths caused by high deceleration, PCF_VSCP was set as the first constraint at a maximum limit of 5720 kN, which was derived from the value of the cross-point of the four curves in Figure 17a. EA_FE was set as the second constraint at a minimum limit of 0.213 MJ obtained from cross-point

in Figure 17b. Furthermore, four design parameters all changed from 5 to 14 mm in the multiobjective optimization design (MOD). The multiobjective optimization problem can be written in the following form:

$$
\begin{cases}
Minmize(-SEA\_VSCP, S\_In) \\
s.t.EA\_FE(A, B, C, D) \geqslant 213kJ \\
\quad PCF\_VSCP \leqslant 5720kN \\
\quad 5mm \leqslant A \leqslant 14mm \\
\quad 5mm \leqslant B \leqslant 14mm \\
\quad 5mm \leqslant C \leqslant 14mm \\
\quad 5mm \leqslant D \leqslant 14mm
\end{cases}
\tag{7}
$$

The flowchart of crashworthiness optimization for VSCP is illustrated in Figure 19, and an multiobjective optimization design was performed based on GRSM and accurate surrogate models. The Pareto frontier of two conflicting objectives (SEA_VSCP and S_In) was obtained through GRSM. Finally the optimal result was selected using grey relational analysis method.
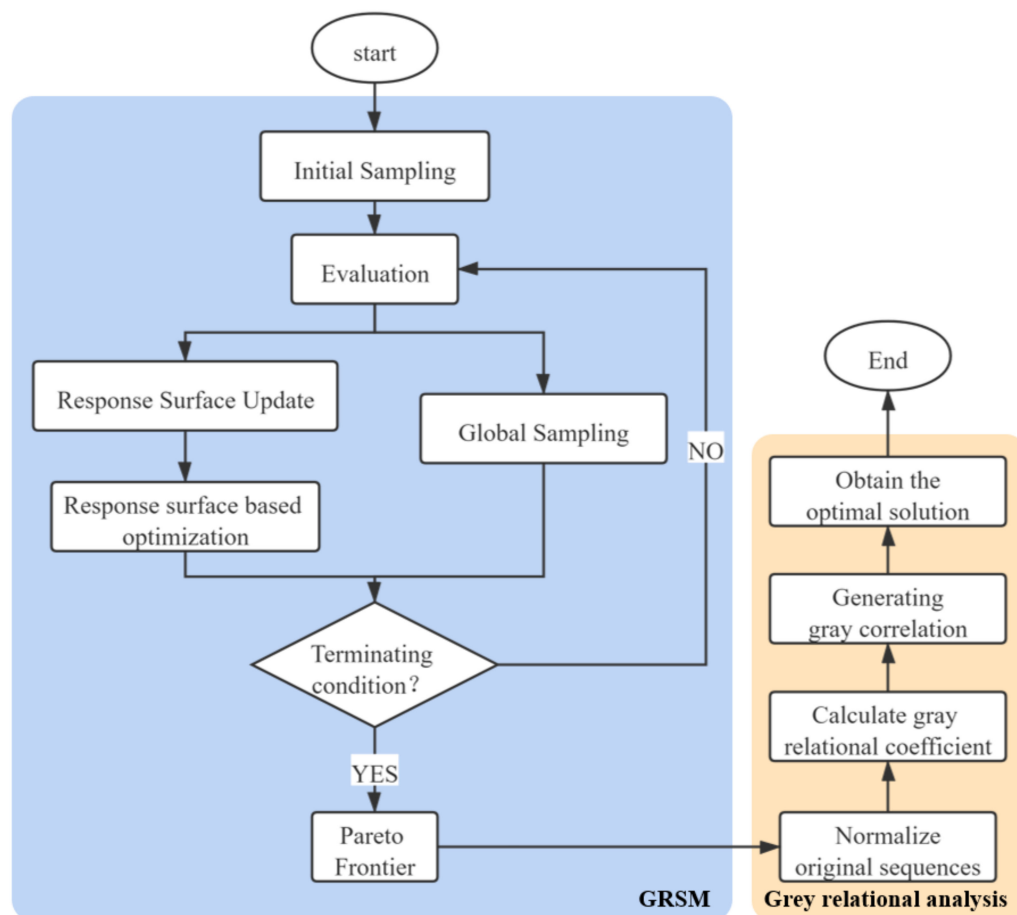


**Figure 19.** Flowchart of crashworthiness optimization for VSCP.

### 5.2. Grey Relational Analysis Method

Grey system theory is a new technology for prediction, relationship analysis and decision-making in many fields [31]. Its basic idea is to determine whether the connection is tight by determining the similarity of the geometric shape between the reference sequence and multiple comparison sequence. It reflects the correlation degree between the curves.

The grey relational analysis with four primary steps to acquire the trade-off from the Pareto frontier [32–34] is as follows:

(1) Determining the analysis sequence Provided that there are m evaluation objects and n evaluation indicators, the reference sequences are listed as $x_0 = \{x_0(k)|k = 1, 2, \ldots, n\}$, and the comparison sequence is $x_0 = \{x_i(k)|k = 1, 2, \ldots, n\}, i = 1, 2, \ldots, m$.

(2) Normalization of variables The original response sequences are normalized into comparable sequences because the data of the original sequence are different in dimension. In this paper, SEA_VSCP belongs to the larger the better response characteristic, S_In belongs to the smaller the better response characteristic. For SEA_VSCP, Equation (9) is more suitable because of larger-better. For S_In, Equation (10) is more suitable because of smaller-better [35]:

$$x_i{}'(k) = \frac{x_i(k) - \min x(k)}{\max x(k) - \min x(k)} \tag{8}$$

$$x_i{}'(k) = 1 - \frac{x_i(k) - \min x(k)}{\max x(k) - \min x(k)} \tag{9}$$

(3) Calculating the grey relational coefficient.

$$\xi_i(k) = \frac{\min\limits_{s}\min\limits_{t}|x_0(t) - x_s(t)| + \rho\max\limits_{s}\max\limits_{t}|x_0(t) - x_s(t)|}{|x_0(k) - x_i(k)| + \rho\max\limits_{s}\max\limits_{t}|x_0(t) - x_s(t)|} \tag{10}$$

$\xi_i(k)$ is the correlation coefficient between the comparison sequence $x_i$ and the reference sequence $x_0$ on the $k$th evaluation index. $\rho(\rho \in [0, 1])$ represents the degree of resolution, which means that the smaller $\rho$ is, the greater the resolution is. In this study, the value of $\rho$ is set to 0.5.

(4) Generating grey correlation. Grey correlation is generated by concentrating the grey relational coefficient into a single sequence, which can be formulated as:

$$r_i = \frac{1}{n}\sum_{k=1}^{n}\xi_i(k) \tag{11}$$

where $r_i$ is the grey weighted correlation of the $i$th evaluation object to the ideal object.

### 5.3. Results and Confirmations

The Pareto frontier for crashworthiness optimization problem of VSCP is plotted as red circles in Figure 20.
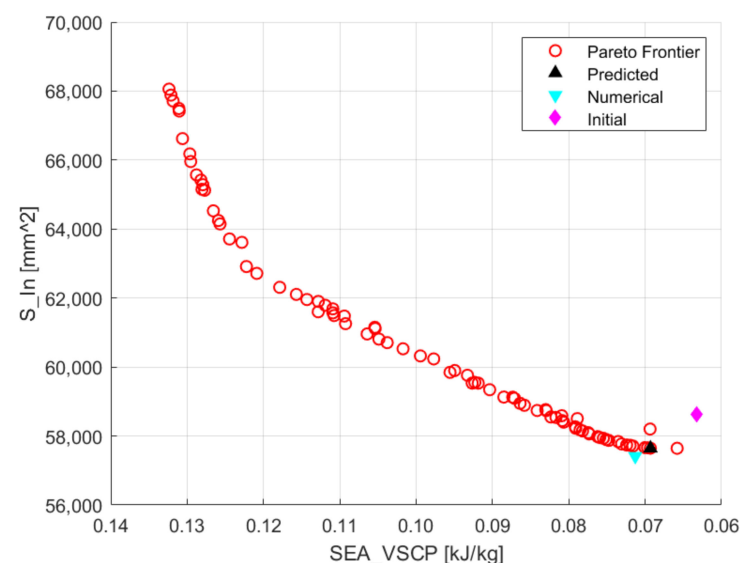


**Figure 20.** Pareto frontier of the multiobjective optimization.

The optimal solution is found by the gray relational analysis method, which can strike the desired balance between SEA_VSCP and S_In. Therefore, the relational coefficients and grey correlation are listed in Table 7. According to the grey correlation weighting, the evaluation objects can be sorted, and the correlation sequence of the evaluation objects can be established. The optimum values are obtained with the highest grey correlation weighting of 0.6725 and the values of the design variables A, B, C and D are 8.27, 13.99, 11.81 and 8.34 mm, respectively.

**Table 7.** Grey correlation analytical data (top ten).

| Original Sequences | | Normalized Data | | Relational Coefficient | | Grey Correlation |
|---|---|---|---|---|---|---|
| S_In (mm$^2$) | SEA_VSCP (kJ) | S_In (mm$^2$) | SEA_VSCP (kJ) | S_In (mm$^2$) | SEA_VSCP (kJ) | Weighting |
| 57,648.0200 | 0.0693 | 0.0527 | 0.9997 | 0.3455 | 0.9994 | 0.6725 |
| 57,663.8630 | 0.0700 | 0.0632 | 0.9982 | 0.3480 | 0.9964 | 0.6722 |
| 57,660.4640 | 0.0697 | 0.0582 | 0.9985 | 0.3468 | 0.9971 | 0.6719 |
| 57,709.9750 | 0.0716 | 0.0871 | 0.9938 | 0.3539 | 0.9877 | 0.6708 |
| 57,739.2350 | 0.0724 | 0.0995 | 0.9910 | 0.3570 | 0.9822 | 0.6696 |
| 57,731.3230 | 0.0720 | 0.0926 | 0.9917 | 0.3553 | 0.9837 | 0.6695 |
| 57,770.3390 | 0.0731 | 0.1093 | 0.9880 | 0.3595 | 0.9765 | 0.6680 |
| 68,055.7860 | 0.1324 | 1.0000 | 0.0000 | 1.0000 | 0.3333 | 0.6667 |
| 57,645.1180 | 0.0658 | 0.0000 | 1.0000 | 0.3333 | 1.0000 | 0.6667 |
| 67,882.4910 | 0.1321 | 0.9962 | 0.0166 | 0.9924 | 0.3371 | 0.6647 |

To validate the optimal result, numerical simulations of these optimal points were performed. The predicted responses are extracted from RS surrogate model, and the numerical responses are obtained from FEM calculations.

The contrast between the numerical result and predicted result is displayed in Table 8 and the comparison among numerical, predicted and initial responses is shown in Figure 20. It can be distinctly seen that the optimal result based on the RS surrogate models is in reasonable agreement with the numerical results offered by the FEM.

**Table 8.** Confirmation of optimal solution.

| Optimum | | Optimal Points |
|---|---|---|
| A (mm) | | 8.27 |
| B (mm) | | 13.99 |
| C (mm) | | 11.81 |
| D (mm) | | 8.34 |
| SEA_VSCP (kg/kJ) | Numerical | 0.0713 |
| | Predicted | 0.0693 |
| | Error (%) | 2.81 |
| S_In (mm$^2$) | Numerical | 57,413.441 |
| | Predicted | 57,645.807 |
| | Error (%) | 0.40 |

As shown in Table 9, compared to USCP, the specific energy absorption of VSCP significantly increased by 12.82%. The area of intrusion slightly decreased by 2.05%, and the displacements contrast of 10 markers between VSCP and USCP are shown in Table 10. In addition, the PCF_VSCP is 5731.450 kN that is a little bit higher than 5720 kN of USCP, which indicates that the influence on PCF is almost same between VSCP and USCP. The EA_FE is 0.214 MJ that is higher than 0.208 MJ of USCP.

**Table 9.** Difference between the optimal structure and initial structure.

| | SEA_VSCP (kg/kJ) | S_In (mm$^2$) |
|---|---|---|
| Initial structure | 0.0632 | 58,617.700 |
| Optimal structure | 0.0713 | 57,413.441 |
| Difference (%) | 12.82 | 2.05 |

**Table 10.** Displacement contrast of 10 markers between VSCP and USCP.

|   | VSCP (mm) | USCP (mm) |
|---|---|---|
| A | 1.431 | 1.742 |
| B | 15.976 | 15.483 |
| C | 30.031 | 28.800 |
| D | 31.739 | 32.745 |
| E | 30.147 | 31.318 |
| F | 24.670 | 25.670 |
| G | 19.796 | 20.622 |
| H | 13.962 | 14.575 |
| I | 7.399 | 7.797 |
| J | 2.499 | 2.773 |

From the contrast between VSCP and USCP, a higher SEA_VSCP means a higher material utilization rate which is parallel with lightweight design; a lower S_In means higher occupants living space and indicates that VSCP was in a better state of protection. A higher EA_FE expresses that more impact energy is dissipated by the front-end structure of subway, which is helpful to protect supporting structure and car body from destruction. Consequently, the VSCP structure with optimum parameters has a better performance than USCP on crashworthiness.

## 6. Conclusions

In this paper, the study of USCP was performed with experiment and finite element analysis methods. Based on the validated FEM, VSCP was proposed and analyzed to improve the crashworthiness. To obtain the optimum stiffness designs of this structure, MOD carried out with the variables A, B, C and D as well as objective functions of S_In and SEA_VSCP with GRSM algorithm. The following are the summarized conclusions resulting from this study:

- A dynamic crash experiment was performed on USCPs assembled in cab car front-end structure with an impact mass of 24,662 kg and an impact velocity of 4.69 m/s, and the cab car front-end structure absorbed a total of 0.213 MJ. The displacement at the impact point was 37 mm, which was also the maximum displacement on the collision post, and the living space had not been destroyed.
- Compared with parameter A, parameters B, C and D with larger slopes have more distinct effects on the S_In response. With increasing variables B, C and D (the thickness of all the parts of VSCP), the curves of the S_In response began to decline distinctly and then increase slightly. The curve of the S_In response undergoes a slight decline and then a relatively significant increase.
- The degree of effects on SEA_VSCP are D, A, C, and B in order of highest to lowest. The value of SEA_VSCP decreases with increasing variables A and D, and the slopes of the effect curves of variables B and C are near zero, which indicates that these two variables have little effect on SEA_VSCP.
- Based on the MOD, the VSCP achieved better crashworthiness than the USCP. Studies have found that these two goals may conflict with each other and usually do not achieve the optimal results at the same time, which has been proven in other studies, e.g., Refs. [36–39]. The optimal result determined by the grey relational analysis method in the Pareto frontier shows that an improving of 12.82% on SEA_VSCP response and an increasing of 0.57% on S_In response.

**Author Contributions:** Conceptualization, W.G. and P.X.; methodology, W.G, P.X. and C.Y.; software, W.G.; investigation, W.G.; resources, W.G.; experiment, W.G., J.X., H.Z. and Z.Y.; data curation, W.G. and C.Y.; writing—original draft preparation, W.G.; writing—review and editing, W.G. and C.Y.; project administration, P.X.; funding acquisition, P.X. and C.Y. All authors have read and agreed to the published version of the manuscript.

**Institutional Review Board Statement:** Not applicable.

**Informed Consent Statement:** Not applicable.

**Data Availability Statement:** Not applicable.

**Conflicts of Interest:** The authors declare no conflict of interest.

## Abbreviations

| | |
|---|---|
| VSCP | Variable stiffness collision post |
| USCP | Uniform stiffness collision post |
| SEA | Specific energy absorption |
| SEA_VSCP | The specific energy absorption of VSCP |
| S_In | Area of intrusion response |
| PCF | Peak crash force |
| PCF_VSCP | Peak crash force of VSCP |
| EA | Energy absorption |
| EA_FE | Energy absorption of the front-end of cab car |
| FEM | Finite element model |
| DOE | Design of experiment |
| RS | Response surface |
| GRSM | Global response search method |
| MOD | Multiobjective optimization design |

## Appendix A  Polynomial Functions of SEA_VSCP and S_In

The full quadratic polynomial functions of SEA_VSCP and S_In in this study are provided as follows:

$$
\begin{aligned}
\text{SEA\_VSCP} = {}& 0.2808 - 0.0105A - 0.0023B - 0.00197C - 0.0222D + 1.2859 \times 10^{-4}A^2 \\
& -3.1135 \times 10^{-5}B^2 + 5.0416 \times 10^{-6}C^2 + 5.6451 \times 10^{-4}D^2 \\
& +4.9224 \times 10^{-5}AB + 1.0015 \times 10^{-4}AC + 4.166 \times 10^{-4}AD \\
& +6.2127 \times 10^{-5}BC + 1.6322 \times 10^{-4}BD - 3.6518 \times 10^{-6}CD
\end{aligned}
$$

$$
\begin{aligned}
\text{S}_{\text{In}} = {}& 87248.5849 - 408.7959A - 789.2253B - 1771.5885C - 1791.6982D \\
& +53.9643A^2 + 46.1455B^2 + 114.2593C^2 + 100.2208D^2 + 5.7734AB \\
& -42.6702AC - 13.3778AD - 33.6918BC - 26.3110BD - 19.1532CD
\end{aligned}
$$

## References

1. Xu, P.; Xu, K.; Yao, S.; Yang, C.; Huang, Q.; Zhao, H.; Xing, J. Parameter study and multi-objective optimisation of an axisymmetric rectangular tube with diaphragms for subways. *Thin-Walled Struct.* **2019**, *136*, 186–199. [CrossRef]
2. Baykasoğlu, C.; Sünbüloğlu, E.; Bozdağ, S.E.; Aruk, F.; Toprak, T.; Mugan, A. Railroad passenger car collision analysis and modifications for improved crashworthiness. *Int. J. Crashworthiness* **2011**, *16*, 319–329. [CrossRef]
3. Lei, C.; Xiao, S.; Luo, S.; Zhang, Z. State-of-the-art research development of rail vehicles crashworthiness. *J. China Railw. Soc.* **2013**, *35*, 31–40.
4. Lu, G. Energy absorption requirement for crashworthy vehicles. *Proc. Inst. Mech. Eng. Part F J. Rail Rapid Transit* **2002**, *216*, 31–39. [CrossRef]
5. Sun, G.; Guo, X.; Li, S.; Ruan, D.; Li, Q. Comparative study on aluminum/GFRP/CFRP tubes for oblique lateral crushing. *Thin-Walled Struct.* **2020**, *152*, 106420. [CrossRef]
6. Sun, G.; Kong, X.; Wang, Z.; Luo, Q.; Li, Q. Experimental investigation into stamping of woven CF/PP laminates: Influences of molding temperature on thermal, mesoscopic and macroscopic properties. *Compos. Struct.* **2021**, *263*, 113507. [CrossRef]
7. Sun, G.; Wang, E.; Zhao, T.; Zheng, G.; Li, Q. Inverse identification of cell-wall material properties of closed-cell aluminum foams based upon vickers nano-indentation tests. *Int. J. Mech. Sci.* **2020**, *176*, 105524. [CrossRef]

8.  Sun, G.; Huo, X.; Wang, H.; Hazell, P.J.; Li, Q. On the structural parameters of honeycomb-core sandwich panels against low-velocity impact. *Compos. Part B Eng.* **2021**, *216*, 108881. [CrossRef]
9.  Chen, D.; Sun, G.; Jin, X.; Li, Q. Quasi-Static Bending and Transverse Crushing Behaviors for Hat-Shaped Composite Tubes Made of CFRP, GFRP and Their Hybrid Structures. *Compos. Struct.* **2020**, *239*, 111842. [CrossRef]
10. Wikipedia. Washington Metro Train Collision. 2009. Available online: https://en.jinzhao.wiki/wiki/June_2009_Washington_Metro_train_collision (accessed on 21 October 2021).
11. Xie, S.; Zhou, H. Impact characteristics of a composite energy absorbing bearing structure for railway vehicles. *Compos. Part B Eng.* **2014**, *67*, 455–463. [CrossRef]
12. Xu, P.; Yang, C.; Peng, Y.; Yao, S.; Xing, J.; Li, B. Cut-out grooves optimization to improve crashworthiness of a gradual energy-absorbing structure for subway vehicles. *Mater. Des.* **2016**, *103*, 132–143. [CrossRef]
13. Xie, S.; Liang, X.; Hui, Z.; Jian, L. Crashworthiness optimisation of the front-end structure of the lead car of a high-speed train. *Struct. Multidiscip. Optim.* **2015**, *53*, 339–347. [CrossRef]
14. Lu, Z.; Li, B.; Yang, C.; Zhao, H.; Xu, P.; Yao, S.; Peng, Y.; Zhang, D. Numerical and experimental study on the design strategy of a new collapse zone structure for railway vehicles. *Int. J. Crashworthiness* **2017**, *22*, 488–502. [CrossRef]
15. Xu, P.; Xing, J.; Yao, S.; Yang, C.; Chen, K.; Li, B. Energy distribution analysis and multi-objective optimization of a gradual energy-absorbing structure for subway vehicles. *Thin-Walled Struct.* **2017**, *115*, 255–263. [CrossRef]
16. Yang, C.; Xu, P.; Yao, S.; Xie, S.; Li, Q.; Peng, Y. Optimization of honeycomb strength assignment for a composite energy-absorbing structure. *Thin-Walled Struct.* **2018**, *127*, 741–755. [CrossRef]
17. Peng, Y.; Hou, L.; Che, Q.; Xu, P.; Li, F. Multi-objective robust optimization design of a front-end underframe structure for a high-speed train. *Eng. Optim.* **2019**, *51*, 753–774. [CrossRef]
18. Xing, J.; Xu, P.; Yao, S.; Zhao, H.; Huang, Q.; Xu, K.; Li, B. Crashworthiness optimisation of a step-like bi-tubular energy absorber for subway vehicles. *Int. J. Crashworthiness* **2020**, *25*, 252–262. [CrossRef]
19. Gao, G.; Zhuo, T.; Guan, W. Recent research development of energy-absorption structure and application for railway vehicles. *J. Cent. South Univ.* **2020**, *27*, 1012–1038. [CrossRef]
20. Xing, J.; Xu, P.; Zhao, H.; Yao, S.-G.; Wang, Q.-X.; Li, B.-H. Crashworthiness design and experimental validation of a novel collision post structure for subway cab cars. *J. Cent. South Univ.* **2020**, *27*, 2763–2775. [CrossRef]
21. Kang, R. Design and Analysis Cab FXD3 Passenger Electric Locomotive. Master's Thesis, Dalian University of Technology, Dalian, China, 2019.
22. Liu, H.; Wang, K.; Luo, Q.; Zhao, G.; Zhang, C.; Li, X. Research on the elastic-plastic of collision post for metro vehicles based on ASME standard. *J. Dalian Jiaotong Univ.* **2017**, *38*, 46–49.
23. Tyrell, D.C.; Severson, K.J.; Mayville, R.A.; Stringfellow, R.G.; Berry, S.; Perlman, A.B. Evaluation of cab car crashworthiness design modifications. In Proceedings of the 1997 IEEE/ASME Joint Railroad Conference, Boston, MA, USA, 18–20 March 1997; pp. 49–58.
24. Mayville, R.A.; Hammond, R.P.; Johnson, K.N. Static and dynamic crush testing and analysis of a rail vehicle corner structural element. In Proceedings of the 8th ASME Symposium on Crashworthiness, Occupant Protection and Biomechanics in Tranportation, Nashville, TN, USA, 14–19 November 1999; pp. 51–67.
25. Song, X.; Sun, G.; Li, G.; Gao, W.; Li, Q. Crashworthiness optimization of foam-filled tapered thin-walled structure using multiple surrogate models. *Struct. Multidisc. Optim.* **2013**, *47*, 221–231. [CrossRef]
26. Xiang, Y.; Yu, T.; Yang, L. Comparative analysis of energy absorption capacity of polygonal tubes, multi-cell tubes and honeycombs by utilizing key performance indicators. *Mater. Des.* **2016**, *89*, 689–696. [CrossRef]
27. Xu, P.; Yang, C.; Peng, Y.; Yao, S.; Zhang, D.; Li, B. Crash performance and multi-objective optimization of a gradual energy-absorbing structure for subway vehicles. *Int. J. Mech. Sci.* **2016**, *107*, 1–12. [CrossRef]
28. Riazi, S.; Feizi, M.; Hpsseini Tehrani, P. Improving crashworthiness in railcar against rollover. *Trans.-Can. Soc. Mech. Eng.* **2012**, *36*, 383. [CrossRef]
29. Martinez, E.; Tyrell, D.; Zolock, J. Rail-car impact tests with steel coil: Car crush. In Proceedings of the 2003 IEEE/ASME Joint Railroad Conference, Chicago, IL, USA, 24 April 2003; pp. 63–72.
30. Ferreira, S.L.C.; Bruns, R.E.; Ferreira, H.S.; Matos, G.D.; David, J.M.; Brandão, G.C.; da Silva, E.G.P.; Portugal, L.A.; dos Reis, P.S.; Souza, A.S.; et al. Box-behnken design: An alternative for the optimization of analytical methods. *Anal. Chim. Acta* **2007**, *597*, 179–186. [CrossRef]
31. Tosun, N. Determination of optimum parameters for multi-performance characteristics in drilling by using grey relational analysis. *Int. J. Adv. Manuf. Technol.* **2006**, *28*, 450–455. [CrossRef]
32. Sinha, K. Reliability-based multiobjective optimization for automotive crashworthiness and occupant safety. *Struct. Multidisc. Optim.* **2007**, *33*, 255–268. [CrossRef]
33. Pragadish, N.; Pradeep Kumar, M. Optimization of dry EDM process parameters using grey relational analysis. *Arab J. Sci. Eng.* **2016**, *41*, 4383–4390. [CrossRef]
34. Lin, J.L.; Lin, C.L. The use of the orthogonal array with grey relational analysis to optimize the electrical discharge machining process with multiple performance characteristics. *Int. J. Mach. Tools Manuf.* **2002**, *42*, 237–244. [CrossRef]
35. Yu, K.; Liu, Y.; Zhang, Z. Energy-absorbing analysis and reliability-based multiobjective optimization design of graded thickness B pillar with grey relational analysis. *Thin-Walled Struct.* **2019**, *145*, 106364. [CrossRef]

36. Baroutaji, A.; Gilchrist, M.D.; Smyth, D.; Olabi, A.G. Analysis and optimization of sandwich tubes energy absorbers under lateral loading. *Int. J. Impact Eng.* **2015**, *82*, 74–88. [CrossRef]
37. Hou, S.; Li, Q.; Long, S.; Yang, X.; Li, W. Design optimization of regular hexagonal thin-walled columns with crashworthiness criteria. *Finite Elem. Anal. Des.* **2007**, *43*, 555–565. [CrossRef]
38. Hou, S.; Li, Q.; Long, S.; Yang, X.; Li, W. Multiobjective optimization of multi-cell sections for the crashworthiness design. *Int. J. Impact Eng.* **2008**, *35*, 1355–1367. [CrossRef]
39. Ebrahimi, S.; Vahdatazad, N. Multiobjective optimization and sensitivity analysis of honeycomb sandwich cylindrical columns under axial crushing loads. *Thin-Walled Struct.* **2015**, *88*, 90–104. [CrossRef]